

Please cite the Published Version

Zhang, Meng, Sun, Yuzhuo, Meng, Chenchen, Xu, Qijun, Zhang, Yang , Li, Xiaohong , Fan, Louzhen , Li, Tengfei  and Li, Yunchao  (2025) Electrodeposition of oxyanion films as universal chloride ion-repelling layers for efficient and stable seawater oxidation at ampere-level current density. *Journal of Materials Chemistry A*. ISSN 2050-7488

DOI: <https://doi.org/10.1039/D4TA09017A>

Publisher: Royal Society of Chemistry (RSC)

Version: Accepted Version

Downloaded from: <https://e-space.mmu.ac.uk/638988/>

Usage rights:  [Creative Commons: Attribution 4.0](https://creativecommons.org/licenses/by/4.0/)

Additional Information: This is an author-produced version of the published paper. Uploaded in accordance with the University's Research Publications Policy.

Data Access Statement: The data supporting this article have been included as part of the Experimental section and ESI.

Enquiries:

If you have questions about this document, contact openresearch@mmu.ac.uk. Please include the URL of the record in e-space. If you believe that your, or a third party's rights have been compromised through this document please see our Take Down policy (available from <https://www.mmu.ac.uk/library/using-the-library/policies-and-guidelines>)

Electrodeposition of oxyanion films as universal chloride ions-repelling layers for efficient and stable seawater oxidation at ampere-level current density

Received 00th January 20xx,
Accepted 00th January 20xx

DOI: 10.1039/x0xx00000x

Meng Zhang^a, Yuzhuo Sun^a, Chenchen Meng^a, Qijun Xu^a, Yang Zhang^a, Xiaohong Li^a, Louzhen Fan^a, Tengfei Li^{*b}, Yunchao Li^{*a}

Seawater splitting is an environmentally friendly pathway for hydrogen production, helping to resolve the conflict between the growing hydrogen energy demand and freshwater scarcity. However, abundant chloride ions in seawater cause chlorine oxidation reactions (CIOR), leading to severe anode corrosion and increased energy consumption. We developed an oxyanion film electrodeposition strategy to form a universal Cl⁻-repelling layer onto electrocatalyst surfaces, allowing efficient and stable seawater oxidation at high current densities. Among several oxyanion films (sulfate, phosphate and carbonate), the Ni-Co layered double hydroxides catalyst with sulfate modification (NiCo-LDH@Sulfate) demonstrated the best seawater oxidation activity and stability (1 A cm⁻² with 381 mV overpotential; stable activity at 600 mA cm⁻² for 330 hours). In-depth explorations indicate that the high electrostatic potential generated by the oxyanion films can effectively repel Cl⁻ and inhabit CIOR. The oxyanion films can also improve oxygen evolution reaction (OER) activity by accelerating the generation of the OER active centers and changing the coordination intensity between the catalytic centers and the OER intermediates. Impressively, this strategy enables ultrafast formation of protective layer within 5 min and can be applied to a wide range of OER array electrodes, thus providing groundbreaking guidance for the industrialization of seawater splitting.

1. Introduction

The conflict between freshwater scarcity and the rapid development of hydrogen energy has sparked growing interests in using seawater as a medium for electrocatalytic production of green hydrogen (H₂).¹⁻⁸ Despite the attractive prospect of converting seawater into H₂, it imposes higher demands on the design of electrocatalysts, particularly for the anodic oxygen evolution reaction (OER).⁹⁻¹² As seawater contains chloride ions (Cl⁻) with concentrations typically greater than 0.5 M, which means that chloride oxidation reaction (CIOR) may also occur at the anode during seawater electrolysis in addition to OER.¹³⁻¹⁵ Although the oxidation of Cl⁻ into chlorine gas or HOCl/OCl⁻ (E₀ = 1.48 V vs. Reversible Hydrogen Electrode, RHE) is thermodynamically less favorable than OER (E₀ = 1.23 V vs. RHE) under alkaline conditions, the high concentration of Cl⁻ in the electrolyte can still disorderly intercalate into the catalysts and lead to continuous structural collapse and loss of metal ions through surface adsorption.¹⁵⁻¹⁹ Additionally, CIOR also consumes energy as a competing reaction to the OER, thus increasing the energy input required for the anode process and

affecting catalytic activity.²⁰⁻²¹ The harsh reaction during seawater splitting poses high demands on the catalytic activity, OER selectivity and corrosion resistance of the catalyst, presenting significant challenges for the selection and design of OER catalysts.²²⁻²⁶

Recently, researchers have proposed various strategies to address the challenges in seawater splitting. Wang et al. demonstrated a thermodynamic priority strategy by designing catalysts with an ultralow OER potential (490 mV lower than the theoretical potential of CIOR), effectively avoiding the CIOR process and promoting seawater splitting.²⁷ Xie et al. designed an innovative membrane-based in-situ water purification system, which provides a promising solution for persistent seawater splitting using a self-driven phase transition migration strategy.²⁸ Fan et al. reported an in-situ construction strategy to form a Cl⁻-repelling layer, which utilizes the introduction of carbonate anion intercalation and the surface anchoring of graphene quantum dots to block the adverse adsorption of chloride ions and enable stable and efficient seawater splitting.⁶ Following this game-changing discovery, strategies for in-situ formation of Cl⁻ electrostatic repulsion layers during seawater electrolysis have received considerable attention in recent years.²⁹⁻³³ However, the in-situ repulsion layer formation process typically requires >20 hours, which accounts for ~10% of the overall electrolysis lifespan. Moreover, the in-situ formation of a certain protective layer is usually only applicable to a specific OER catalyst. Therefore, it is imperative to develop a universal surface modification strategy that is applicable to a broad range of OER catalysts and enables a rapid formation of

^a Key laboratory of Theoretical and Computational Photochemistry, Ministry of Education, College of Chemistry, Beijing Normal University, Beijing 100875 (P. R. China). E-mail: liyc@bnu.edu.cn

^b School of Chemistry and Environment, Manchester Metropolitan University, Manchester, M1 5GD, United Kingdom. E-mail: t.li@mmu.ac.uk

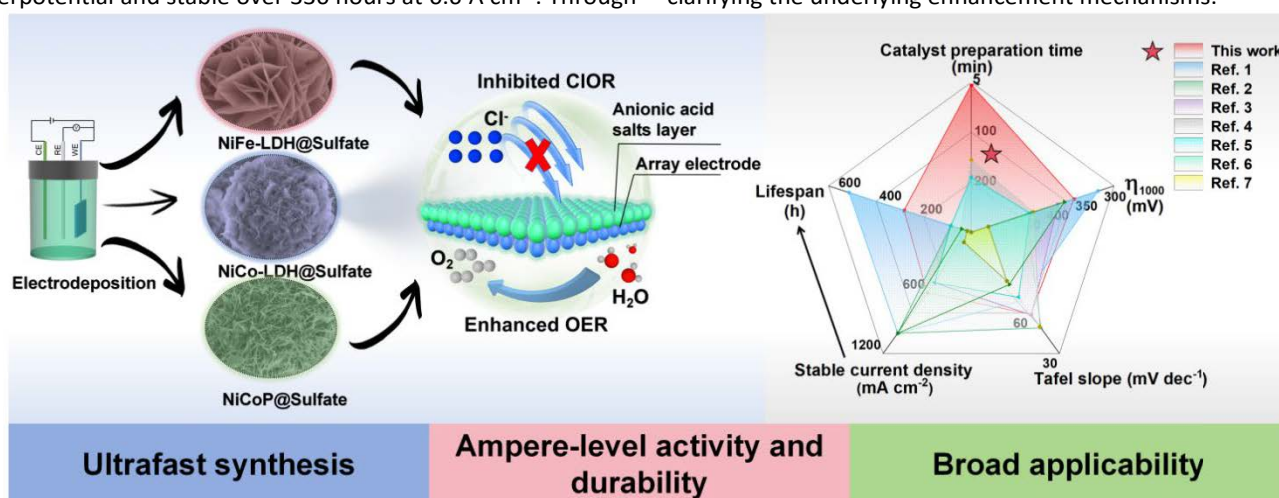
† Supplementary Information available: [details of any supplementary information available should be included here]. See DOI: 10.1039/x0xx00000x

‡ These authors contributed equally to this study.

the Cl^- -repelling layer to achieve long-term and ampere-level OER activity for seawater electrolysis. Besides, a thorough investigation into the effect of such additional layers on Cl^- repulsion and OER activity is also highly desirable to enable a comprehensive and in-depth understanding of this special electrolysis process.

As shown in the Scheme 1, we developed an ultrafast (5 min) electrodeposition method prior to seawater electrolysis to fabricate oxyanion films directly onto the OER electrocatalyst surface, yielding Cl^- -repelling layers for efficient and durable ampere-level current density seawater oxidation. The electrodeposition of a series of oxyanion films (sulfate, phosphate and carbonate) onto different OER catalysts (NiFe-LDH, NiCo-LDH and NiCoP) can significantly inhibit the ClOR process and enhance OER for seawater splitting, among which sulfate modification on NiCo-LDH demonstrated the best electrochemical activity and stability, i.e., 1 A cm^{-2} at 381 mV overpotential and stable over 330 hours at 0.6 A cm^{-2} . Through

this simple surface modification strategy, we can achieve an ideal balance of current density, overpotential, Tafel slope, stability and catalyst preparation time, which outperform (or are comparable to) most of the state-of-the-art seawater OER catalysts (Scheme 1). In-situ spectroscopic characterizations, probe techniques and theoretical calculations indicate that the high surface electrostatic potential of the sulfate film is crucial for repelling Cl^- , thereby inhibiting the ClOR process. Furthermore, the introduction of sulfate can also facilitate the OER process by adjusting the electronic structures of the catalyst, enhancing the surface adsorption of OER intermediates and accelerating the generation of the active centers in the OER catalyst. Notably, this strategy has broad applicability demonstrated for various oxyanions and OER catalysts. This study provides groundbreaking guidance for the industrialization of seawater splitting, by developing effective strategies to enhance the OER catalyst performance and clarifying the underlying enhancement mechanisms.



Scheme 1. Our strategy of using electrodeposited sulfate film as a universal chloride ion exclusion layer, and the comparison with the most advanced reported seawater electrolysis OER catalysts.³⁴⁻⁴⁰

2. Experimental

2.1. Experimental details

Pre-processing of NF: Specifically, a piece of NF ($1.5 \text{ cm} \times 2.0 \text{ cm}$) was first cleaned by HCl solution, acetone, and deionized (DI) water in sequence. Then, the clean NF was dried at $60 \text{ }^\circ\text{C}$ in a vacuum environment for standby.

Synthesis of NiCo-LDH: NiCo-LDH catalysts were prepared according to an established protocol with some modifications.¹³ Typically, $\text{Ni}(\text{NO}_3)_2 \cdot 6\text{H}_2\text{O}$ (0.52 g), $\text{Co}(\text{NO}_3)_2 \cdot 6\text{H}_2\text{O}$ (0.35 g) and $\text{C}_{19}\text{H}_{42}\text{BrN}$ (1 g) were dissolved in a mixed solution of CH_3OH (25 mL) and distilled water (5 mL) under stirring until completely dissolved. The mixed solution was transferred to a 50 mL teflon autoclave and place the pre-treated NF inside, which was then sealed and heated in an oven at $180 \text{ }^\circ\text{C}$ for 24 h. Finally, the obtained NF was washed several times with ethanol and deionized water, and vacuum dried at $60 \text{ }^\circ\text{C}$ to obtain NiCo-LDH.

Synthesis of NiCo-LDH@Sulfate: The electrochemical surface modification process was carried out in the traditional three

electrode mode, with NiCo-LDH as the working electrode, platinum wire as the counter electrode, and Ag/AgCl as the reference electrode. In addition, Na_2SO_4 (1.20 g) was dissolved in 25 mL of distilled water, stirred until completely dissolved, and used as the electrolyte. During the surface modification process, a constant potential of -1.5 V vs. RHE was applied for 150 s, followed by a 180° reversal of the working electrode and continued for 150 s. Finally, wash several times with ethanol and deionized water, and vacuum dry at $60 \text{ }^\circ\text{C}$ to obtain NiCo-LDH@Sulfate.

Synthesis of NiCo-LDH@Phosphate: The synthesis procedure followed the same protocol as that for NiCo-LDH@Sulfate, except that NaH_2PO_4 was used as the electrolyte instead.

Synthesis of NiCo-LDH@Carbonate: The synthesis procedure followed the same protocol as that for NiCo-LDH@Sulfate, except that NaHCO_3 was used as the electrolyte instead.

Synthesis of NiFe-LDH@Sulfate: The synthesis of NiFe-LDH adopted a reported method with some improvements.⁴¹ Typically, $\text{Ni}(\text{NO}_3)_2 \cdot 6\text{H}_2\text{O}$ (0.40 g), $\text{Fe}(\text{NO}_3)_3 \cdot 9\text{H}_2\text{O}$ (0.35 g), $\text{CO}(\text{NH}_2)_2$ (0.60 g) and NH_4F (0.15 g) were dissolved in distilled water (30 mL) under stirring until completely dissolved. The solution was transferred to a 50 mL

teflon autoclave and place the pre treated NF inside, which was then sealed and heated in an oven at 120 °C for 6 h. Finally, the obtained NF was washed several times with ethanol and deionized water, and vacuum dried at 60 °C to obtain NiFe-LDH. The electrochemical surface modification process followed the same procedure as described for the synthesis of NiCo-LDH@Sulfate, except that the working electrode was replaced with NiFe-LDH.

Synthesis of NiCoP@Sulfate: The synthesis of NiCoP adopted a reported method with some improvements.⁴² Typically, Ni(NO₃)₂·6H₂O (0.35 g), Co(NO₃)₂·6H₂O (0.35 g), CO(NH₂)₂ (0.36 g) and NH₄F (0.09 g) were dissolved in distilled water (30 mL) under stirring until completely dissolved. The solution was transferred into

a 50 mL Teflon-lined autoclave, followed by the insertion of the pre-treated NF. The autoclave was then sealed and heated at 120 °C for 10 h in an oven. Finally, the obtained NF was washed several times with ethanol and deionized water, and vacuum dried at 60 °C to obtain NiCoP. The electrochemical surface modification process is the same as Synthesis of NiCo-LDH@Sulfate, but the working electrode is replaced with NiCoP.

2.2. Physical measurements and Electrochemical Measurements

The detailed information is described in the Supplementary Information.

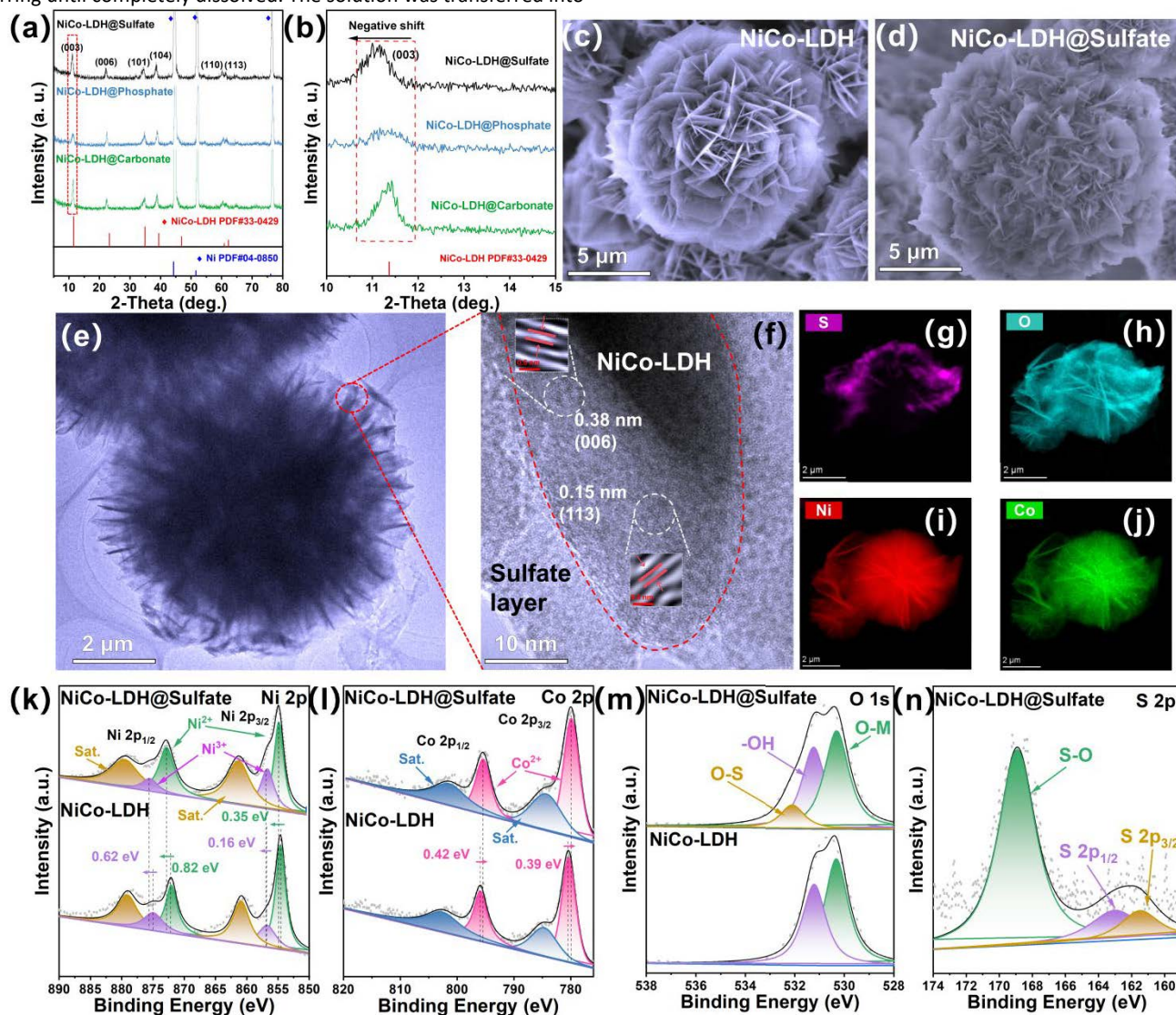


Fig. 1. (a) XRD patterns of NiCo-LDH modified with different oxyanions. (b) Zoom-in XRD patterns of the (003) peak. (c) SEM image of NiCo-LDH. (d-f) SEM image (d), TEM image (e) and HRTEM image (f) of NiCo-LDH@Sulfate. (g-j) EDX-mapping images of NiCo-LDH@Sulfate. (k-n) High-resolution XPS spectra of NiCo-LDH@Sulfate and NiCo-LDH, including Ni 2p (k), Co 2p (l), O 1s (m) and S 2p (n).

3. Results and Discussion

3.1. Oxyanion Film Synthesis and Characterizations

An ultrafast electrodeposition strategy was employed to introduce the oxyanion films onto the surfaces of the OER catalysts. Specifically, the corresponding oxyanion films (sulfate, phosphate, carbonate) were electro-synthesized on the surfaces of NiCo-LDH under constant current mode. To ascertain the formation of different

oxyanion films on the catalyst surfaces, NiCo-LDH electrodes before and after oxyanion modifications were analyzed by Raman spectroscopy. As shown in Fig. S1, the typical vibration peaks of SO_4^{2-} , PO_4^{3-} , and CO_3^{2-} were detected, confirming the successful construction of surface oxyanion films.^{9,43-45} Although only the crystal structure of NiCo-LDH (PDF#33-0429) was observed in the X-ray diffraction (XRD) patterns (Fig. 1a),⁴⁶ the main (003) crystal plane was still shifted to a lower angle upon the introduction of oxyanion films (see the zoom-in XRD in Fig. 1b), which is attributed to the lattice distortion caused by the interaction between NiCo-LDH and the oxyanion films.⁴⁷ Raman spectroscopy and XRD results collectively demonstrated the successful formation of an amorphous oxyanion film. Scanning electron microscopy (SEM) revealed the nanoflower-like structure of NiCo-LDH (Fig. 1c), which is largely retained after modification with sulfate (Fig. 1d). NiCo-LDH modified with other oxyanions also displayed similar surface morphologies (Fig. S2).⁴⁸ The nanoflower-like structure of NiCo-LDH@Sulfate was also confirmed by Transmission Electron Microscopy (TEM) image (Fig. 1e). High-resolution TEM and Selected Area Electron Diffraction (SAED) revealed a clear interface between the crystal and amorphous

phases (Fig. 1f and Fig. S3): the internal lattice fringes align well with the (006) and (113) planes of NiCo-LDH, while the external petals display an amorphous structure, consistent with XRD results.⁴⁹ Energy-dispersive X-ray (EDX) mapping images show a uniform distribution of Ni, Co, and O elements, while the S element is mainly distributed on the surface of the flower-like structure (Fig. 1g-j and Fig. S4a). Additionally, the elemental contents for both the interior and exterior of the core-shell structure were analyzed (Fig. S4b). As shown in Table S1, the sulfate content in the shell is nearly seven times that of the core, confirming the sulfate modification on the surface of NiCo-LDH. Similarly, EDX mappings of NiCo-LDH@Phosphate and NiCo-LDH@Carbonate also reveal the same trend (Fig. S5-S6, Tables S2-S3), highlighting the universality of this electrodeposition strategy for different oxyanions. Notably, the sulfate, phosphate, and carbonate salt films with comparable mass and mass content could be successfully formed onto the NiCo-LDH substrates via optimizing the electrodeposition conditions (eg., precursor concentration, reduction potential and electrodeposition time), as confirmed by weighing (Fig. S7a) and ion chromatography (Fig. S7b) characterizations.

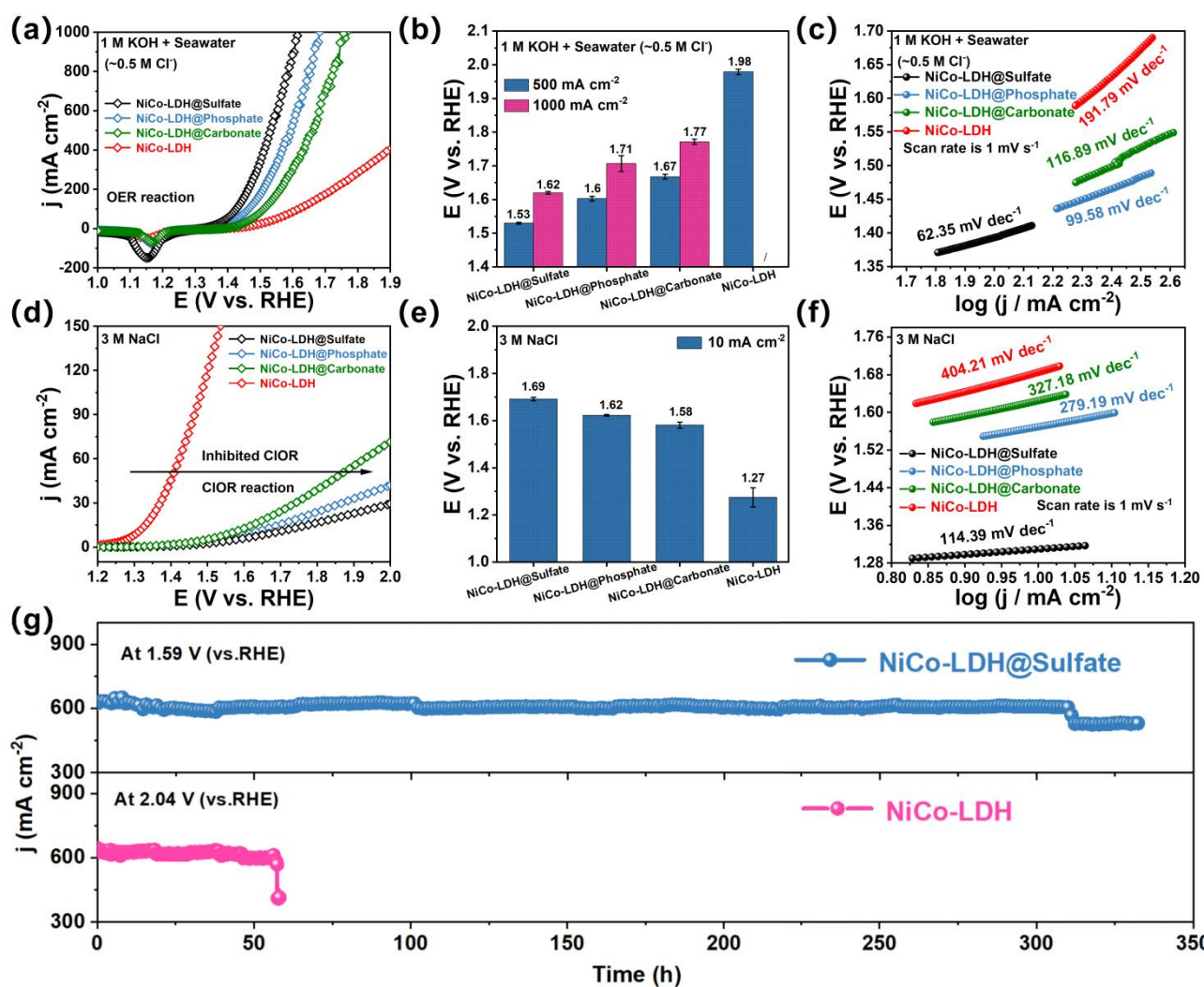


Fig. 2. (a) LSV curves of NiCo-LDH electrodes modified with different oxyanions in 1 M KOH + seawater. (b) The potentials of different catalysts at 500 and 1000 mA cm⁻² in 1 M KOH + seawater (error bars represent triplicate measurements). (c) Tafel studies for different catalysts in 1 M KOH + seawater (scan rate is 1 mV s⁻¹). (d) LSV curves of different catalysts in 3 M NaCl electrolyte. (e) The potentials of different catalysts

at 10 mA cm⁻² in 3 M NaCl electrolyte (error bars represent triplicate measurements). (f) Tafel studies for different catalysts in 3 M NaCl (at a scan rate of 1 mV s⁻¹). (g) Stability tests for NiCo-LDH@Sulfate and NiCo-LDH in 1 M KOH + seawater at a constant potential of 1.59 V and 2.04 V vs. RHE, respectively to achieve similar current density of 600 mA/cm².

The electronic structures and chemical bondings of NiCo-LDH modified with oxyanion films were analyzed by high-resolution X-ray photoelectron spectroscopy (XPS, Fig. 1k-l). Upon the surface modification with sulfate film, the peaks for Ni²⁺ (854.71 eV and 872.78 eV) and Ni³⁺ (856.77 eV and 875.44 eV) were shifted positively,⁵⁰ whereas the peaks for Co²⁺ (779.98 eV and 795.5 eV) were negatively shifted. These observations indicated that the surface bonding of sulfate can regulate the electronic structures of NiCo-LDH and promote the electron transfer from Ni to Co.⁵¹ Additionally, O 1s spectra display a O-S characteristic peak (532.11 eV) signal after sulfate modification (Fig. 1m), and the S 2p spectra are dominated by S-O feature peaks (168.94 eV), which confirm the presence of sulfate in the system (Fig. 1n).⁵² The peaks for S 2p_{1/2} at 163.02 eV and S 2p_{3/2} at 161.49 eV indicate the bondings between S and the NiCo-LDH surface.⁵³ The electronic structures and chemical bondings of NiCo-LDH modified with phosphate and carbonate were also analyzed, yielding similar conclusions (Fig. S8-S9).⁵⁴

3.2. OER Performance of Seawater Splitting

The OER activities for the NiCo-LDH modified with oxyanion films were evaluated in alkaline seawater electrolyte ([Cl⁻] ~ 0.5 M, pH = 14; Fig. 2a-b and Fig. S10). NiCo-LDH@Sulfate exhibited the most outstanding OER activity, requiring only 301 mV overpotential to reach 500 mA cm⁻², outperforming NiCo-LDH@Phosphate (373 mV), NiCo-LDH@Carbonate (437 mV) and unmodified NiCo-LDH (749 mV). Moreover, under ampere-level current density conditions, NiCo-LDH@Sulfate continued to show remarkable activities, needing only 381 mV to reach 1 A cm⁻², superior to NiCo-LDH@Phosphate (476 mV) and NiCo-LDH@Carbonate (541 mV), whereas unmodified NiCo-LDH was unable to reach 1 A cm⁻² within the potential window. These results indicate that among the anion-modified electrodes, NiCo-LDH@Sulfate has the best OER activity at ampere-level current density. Its excellent catalytic activity surpasses that of most reported alkaline seawater OER catalysts, including some precious metal catalysts (Table S4). Furthermore, the reaction kinetics of NiCo-LDH modified with oxyanion films were assessed via the Tafel studies. To ensure a more reliable determination of the Tafel slopes for the electrodes in this study, various steady-state polarization techniques were employed for assessment.⁵⁵⁻⁵⁶ First, Tafel slopes of NiCo-LDH@sulfate and other control electrodes were evaluated by slow linear sweep voltammetry (LSV) with a scan rate as low as 1 mV s⁻¹ (Fig. 2c). NiCo-LDH@Sulfate exhibited the smallest Tafel slope of 62.35 mV dec⁻¹, indicating the fastest reaction kinetics, superior to NiCo-LDH@Phosphate (99.85 mV dec⁻¹), NiCo-LDH@Carbonate (116.89 mV dec⁻¹) and unmodified NiCo-LDH (191.79 mV dec⁻¹). To validate this result, all the electrodes were also subjected to multistep chronoamperometry tests (MCT, 1.124–1.624 V vs. RHE, at 0.1 V increments), with the steady-state current densities at the end of each step used to determine the Tafel slopes (Fig. S11-S12). The Tafel slope of NiCo-LDH@Sulfate was calculated to be 97.46 mV dec⁻¹, lower than those of NiCo-LDH@Phosphate (109.49 mV dec⁻¹), NiCo-LDH@Carbonate (121.46 mV dec⁻¹), and unmodified NiCo-LDH (157.72 mV dec⁻¹), exhibiting slightly different values yet a similar trend to the LSV results (Fig. 2c). Meanwhile, we observed that NiCo-

LDH@Sulfate had the lowest charge transfer resistance (R_{ct}) (Fig. S13a and Table S5) and a significantly enhanced electrochemical active surface area, as reflected in cyclic voltammetry (CV) scans (Fig. S13b-f). The enhanced OER activities of these oxyanion-modified electrodes were further evidenced by their turnover frequencies (TOF). The TOF values of NiCo-LDH@Sulfate at a 100 mV overpotential was found to be 0.066 s⁻¹ (Fig. S14), higher than that of NiCo-LDH@Phosphate (0.035 s⁻¹) and NiCo-LDH@Carbonate (0.024 s⁻¹), demonstrating superior instantaneous turnover capability.

To demonstrate the inhabitation of ClOR after modifying NiCo-LDH with oxyanion films, we next conducted electrochemical tests in a high-concentration sodium chloride solution (3 M, pH=7). The high [Cl⁻] ensures that the ClOR occurs preferentially over OER, allowing us to evaluate the ClOR activity of the catalysts.⁵⁷ As shown in Fig. 2d-2e and Fig. S15, the unmodified NiCo-LDH required a potential of 1.27 V to reach 10 mA cm⁻², while NiCo-LDH@Carbonate, NiCo-LDH@Phosphate and NiCo-LDH@Sulfate required much higher potentials to reach the same ClOR current (1.58, 1.62, and 1.69 V, respectively). Clearly, among them, NiCo-LDH@Sulfate exhibited the most effective suppression of ClOR. Furthermore, as illustrated in Fig. 2f, Fig. S16 and Fig. S17, the ClOR-Tafel slopes confirmed that NiCo-LDH@Sulfate displayed the slowest ClOR kinetics (404.21 mV dec⁻¹ by LSV and 323.25 mV dec⁻¹ by MCT), notably slower than NiCo-LDH@Phosphate (327.18 mV dec⁻¹ by LSV and 261.57 mV dec⁻¹ by MCT), NiCo-LDH@Carbonate (279.19 mV dec⁻¹ by LSV and 244.15 mV dec⁻¹ by MCT), and unmodified NiCo-LDH (114.39 mV dec⁻¹ by LSV and 168.78 mV dec⁻¹ by MCT). These observations demonstrated that the surface modification with oxyanion films can impede the ClOR process and enhance the OER process in seawater splitting.

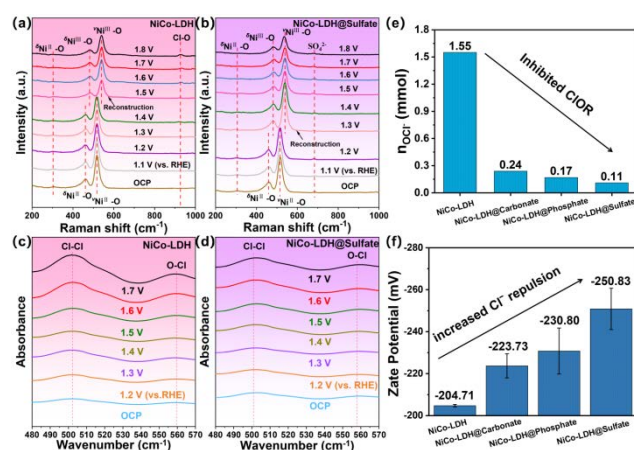


Fig. 3. Experimental evidences to explain the enhanced OER for NiCo-LDH@Sulfate. (a-b) In-situ Raman spectra for NiCo-LDH (a) and NiCo-LDH@Sulfate (b) in 1 M KOH + seawater. (c-d) In-situ infrared spectra for NiCo-LDH (c) and NiCo-LDH@Sulfate (d) in 1 M KOH + seawater. (e) Determination of hypochlorite content in electrolytes after 1-h seawater splitting using different electrodes. (f) The Zeta-potential of NiCo-LDH, NiCo-LDH@Sulfate, NiCo-LDH@Phosphate, NiCo-LDH@Carbonate reflected by dynamic light scattering.

To assess their practical O₂ evolution performances, we further measured the Faradaic efficiency for O₂ production (FE_{O₂}) at 600 mA cm⁻² on NiCo-LDH@Sulfate and other control electrodes, as shown in

Fig. S18. NiCo-LDH@Sulfate exhibited an FE_{O_2} close to 100% in 1 M KOH + seawater (99.71%), much higher than NiCo-LDH@Phosphate (92.71%), NiCo-LDH@Carbonate (84.24%), and unmodified NiCo-LDH (71.63%). The ultrahigh FE_{O_2} demonstrates the potential of NiCo-LDH@Sulfate for practical application in real seawater splitting. The detailed mechanism of this effect will be discussed in depth later.

Long-term stability tests at industrial grade current density were conducted at a constant potential of 1.59 V vs. RHE (Fig. 2g). The NiCo-LDH@Sulfate catalyst could maintain a stable seawater oxidation current density of 600 mA cm^{-2} for over 330 hours without electrolyte recirculation, whereas the unmodified NiCo-LDH could only remain stable for 85 hours before undergoing structural collapse, characterized by a sharp decline in current density due to severe erosion from ClO^- accumulation. The stability of NiCo-LDH@Sulfate surpassed the majority of reported alkaline seawater catalysts (Table S6). The stability was also evaluated by performing CV scans in seawater: the electrochemical activity of NiCo-LDH@Sulfate only decreased by 1.2% after 10,000 CV scans (Fig. S19). The crystal structure and surface morphology of the catalyst exhibited minimal changes after stability tests, as shown in Fig. S20a-c. The Raman spectroscopy (Fig. S20d) showed that the vibration peaks of the surface sulfate film remained unchanged after 10,000 CV scans,

confirming the stable presence of the sulfate film. Furthermore, XPS and EDS spectroscopy were employed to assess the compositional stability of NiCo-LDH@Sulfate before and after the OER stability test (Fig. S21 and Fig. S22). Quantitative analyses of the spectra (Table S7) showed that the element contents of Ni, Co, and S decreased by less than 11% after the stability test, reconfirming the good compositional stability of NiCo-LDH@Sulfate.

3.3. Experimental studies to understand the reasons for efficient and stable seawater oxidation.

The structural evolution of catalyst during the seawater OER process was monitored by in-situ Raman spectroscopy. As shown in Fig. 3a, the characteristic peaks at 460.28 and 517.20 cm^{-1} can be attributed to the ${}^6Ni^{II}-O$ and ${}^vNi^{II}-O$ vibration signals. As the reaction proceeded, the ${}^6Ni^{III}-O$ (481.53 cm^{-1}) and ${}^vNi^{III}-O$ (541.82 cm^{-1}) peaks appeared at 1.5 V vs. RHE for the unmodified NiCo-LDH. This indicates that during the OER process, ${}^6Ni^{II}-O$ and ${}^vNi^{II}-O$ are in-situ reconstructed to ${}^6Ni^{III}-O$ and ${}^vNi^{III}-O$, which have been reported as the main active sites for OER.⁵⁸ More importantly, the gradual appearing of the Cl-O characteristic peak (926.49 cm^{-1}) during the reaction suggested the surface adsorption of Cl-related species on the NiCo-LDH surface that triggers the ClOR process.⁵⁹⁻⁶⁰

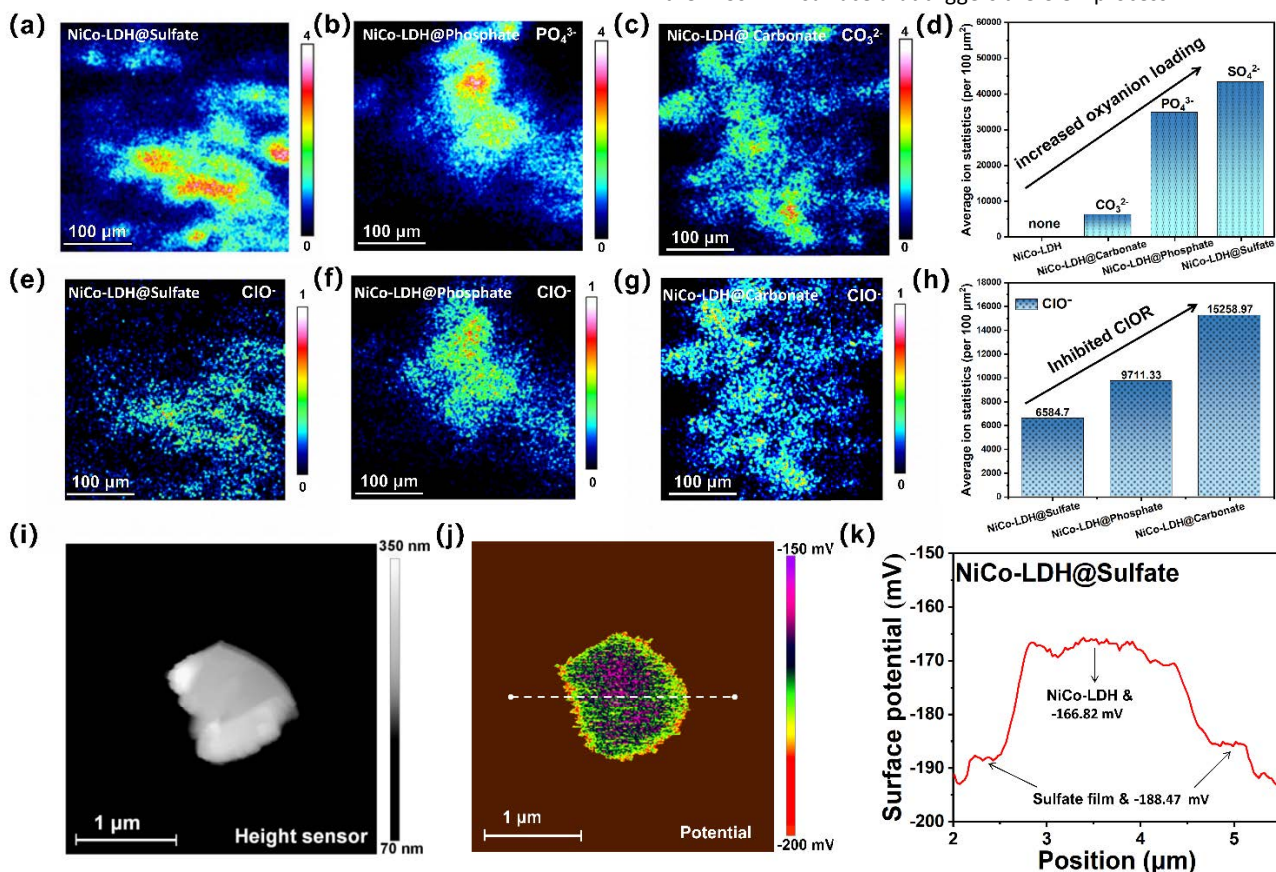


Fig. 4. (a-c) TOF-SIMS images of SO_4^{2-} (a), PO_4^{3-} (b), and CO_3^{2-} (c) on the surfaces of NiCo-LDH electrodes modified with different oxoanion films after activation in 1 M KOH + seawater (Scale: 100 μm). (d) After grinding with Ar plasma for 5 to 15 minutes to clean the electrolyte adsorbed on the surface, negative counts of TOF-SIMS were collected. (e-g) TOF-SIMS images of ClO^- on the surfaces of NiCo-LDH electrodes modified with different oxoanion films after activation in 1 M KOH + seawater. (h) Negative counts of TOF-SIMS were collected. (Scale: 100 μm). (i) AFM image of NiCo-LDH@Sulfate. (j-k) KPFM data of NiCo-LDH@Sulfate, surface potential image (j) and X axis line profile of surface potential (k).

In contrast, the in-situ reconstruction processes for NiCo-LDH@Sulfate, NiCo-LDH@Phosphate, and NiCo-LDH@Carbonate (Fig. 3b and Fig. S23) were completed at potentials of 1.3 V, 1.4 V, and 1.4 V vs. RHE, respectively. Notably, NiCo-LDH@Sulfate demonstrated the lowest reconstruction potential. This suggests that the easier formation of active OER sites may be a key factor contributing to its superior OER activity. Furthermore, no Cl-O related characteristic peaks were found for NiCo-LDH@Sulfate, indicating significantly inhibited ClOR, which is another crucial reason for the enhanced OER activity and stability.

The inhibiting effect of sulfate on ClOR was further investigated by in-situ infrared (IR) spectroscopy via capturing characteristic Cl-Cl/O-Cl signals, as shown in Fig. 3c-d. The absorption bands located around 500 and 560 cm^{-1} can be attributed to the Cl-Cl and O-Cl vibrations, caused by the surface accumulation of Cl-related species during ClOR.⁶¹ These bands were gradually enhanced with increased voltages. The intensity of the Cl-related peaks for NiCo-LDH is significantly higher than that for NiCo-LDH@Sulfate, indicating a higher concentration of chlorine species on the surface of NiCo-LDH and a more facilitated ClOR process.⁶² The in-situ IR and Raman results collectively confirmed that the surface modification with sulfate film can significantly inhibit ClOR. The hypochlorite species (ClO^- , i.e., the main ClOR product) accumulated in the bulk electrolyte after 1 hour of electrolysis was analyzed by using the iodine titration method.⁶³ As shown in Fig. 3e, the hypochlorite generated by NiCo-LDH@Sulfate electrode (0.11 mmol) was lower than that of NiCo-LDH@Phosphate (0.17 mmol), NiCo-LDH@Carbonate (0.24 mmol), and unmodified NiCo-LDH (1.55 mmol). This result implies that the oxyanion modification strategy can indeed suppress the ClOR process, with an inhibiting effect in the order of Sulfate > Phosphate > Carbonate. We hypothesized that this inhibitory mechanism is related to the surface electrostatic potential of the catalyst changed by the oxyanion film. To validate this speculation, we first utilized dynamic light scattering analysis to examine the surface Zeta potential difference between NiCo-LDH@oxyanion film and NiCo-LDH. As shown in Fig. 3f, the surface modification with oxyanion films enhanced the negative charge density on the catalyst surface (lower surface electrostatic potential). The zeta potential for NiCo-LDH@Sulfate was -250.83 mV, significantly lower than that of NiCo-LDH@Phosphate, NiCo-LDH@Carbonate and unmodified NiCo-LDH (-230.80, -223.73 and -204.71 mV, respectively).

In order to explain the difference between the three oxyanion films, the NiCo-LDHs modified with them were characterized by Time of Flight Secondary Ion Mass Spectrometry (TOF-SIMS) mapping to compare the loadings of sulfate, phosphate and carbonate anions (Fig. 4a-c). As expected, strong oxyanion signals were detected on the surfaces of all the NiCo-LDHs. More importantly, the NiCo-LDH@Sulfate was observed to exhibit the highest oxyanion loading among them (much higher than NiCo-LDH@Phosphate and NiCo-LDH@Carbonate, Fig. 4d), thereby leading to the most negative surface electrostatic potential as suggested by the zeta potentials in Fig. 3f. This is attributed to the fact that sulfate has the highest ionization degree in solution⁶⁴ and therefore causes the highest oxyanion loading upon electrolysis. This may directly affect the electrode's electrostatic repulsion against Cl^- , as evidenced by the TOF-SIMS quantification of the ClO^- on the surface after electrochemical activation in alkaline seawater (Fig. 4e-g). The amount of ClO^- generated on NiCo-LDH@Sulfate was much lower

than that of NiCo-LDH@Phosphate and NiCo-LDH@Carbonate, which is consistent with the result of ClO^- accumulated in bulk solution in Fig. 4h.⁶⁵ The surface electrostatic potential of NiCo-LDH@Sulfate was further examined by Kelvin Probe Force Microscopy (KPFM).⁶⁶ Fig. 4i-j depict the height and surface potential of the peeled nanosheets from the catalyst surface on a gold-coated Si substrate. The electrostatic potential of the sulfate-modified surface was notably higher than that of the internal NiCo-LDH. The electrostatic potential of the nanosheet core was measured to be around -166.82 mV, whereas the potential of the outer shell was -188.47 mV (Fig. 4k). In conclusion, in-situ spectroscopic and mass spectroscopic characterizations along with surface probe techniques demonstrated that the high electrostatic potential layer (achieved through oxyanion modification) can effectively suppress ClOR.

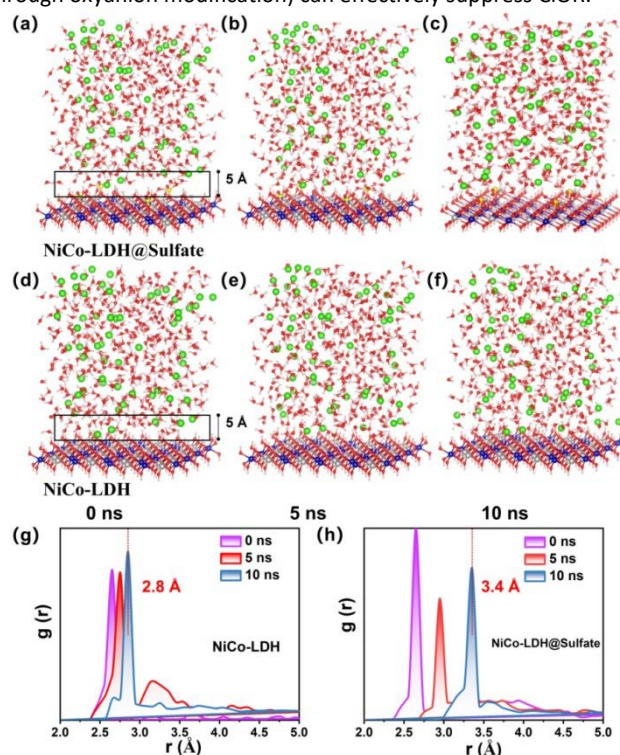


Fig. 5. Mechanistic studies by theoretical calculations. (a-f) Molecular dynamics simulations to study the Cl^- adsorption on NiCo-LDH@Sulfate and NiCo-LDH, and a 10-ns trajectory was accumulated. (g-h) Radial distribution function of the Ni sites on NiCo-LDH and NiCo-LDH@Sulfate in 0-10 ns.

3.4. Theoretical calculations

The mechanism for the ClOR-inhibiting and OER-promoting effects of NiCo-LDH electrode modified with oxyanion films was investigated through molecular dynamics simulations and density functional theory (DFT) calculations. As shown in Fig. S24, starting from a stable NiCo-LDH model, a catalyst model modified with oxyanion was established. In the subsequent molecular dynamic simulations, we considered the atomic surface electrostatic potential and studied the adsorption of Cl^- on the catalyst. A 10-ns trajectory was accumulated, generating dynamic Cl^- -catalyst distance maps (Fig. 5a-f). Meanwhile the temporal changes in radial distribution functions from 0 to 10 ns were recorded (Fig. 5g-h).⁶⁷ Over time, the Cl^- density peaks for NiCo-

LDH were located around a distance of approximately 2.8 Å away from the catalyst interface, whereas on NiCo-LDH@Sulfate, this

distance extends to around 3.4 Å, confirming the sulfate film's ability to repel Cl⁻ ions and therefore reduce the CIOR activity.

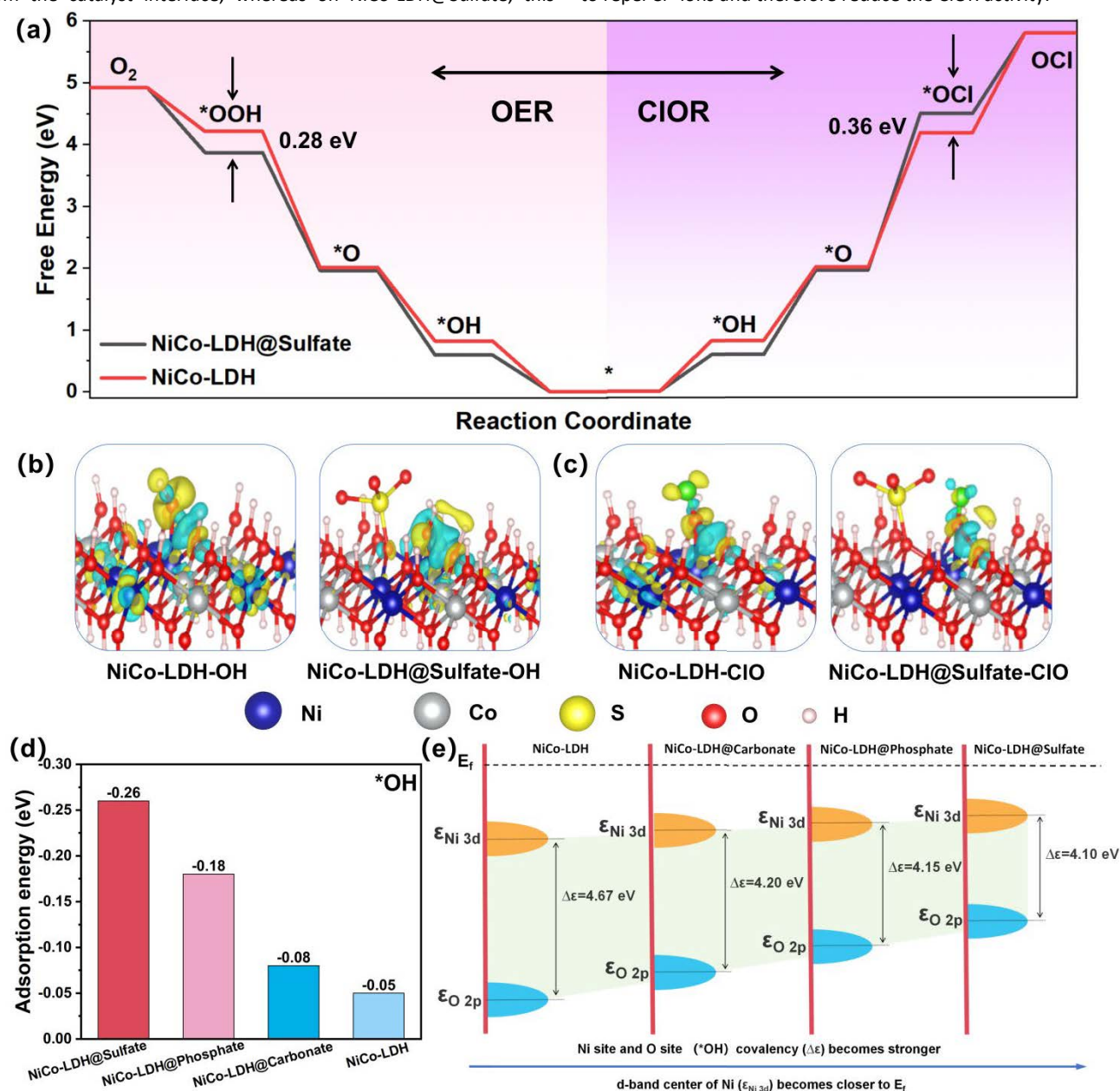


Fig. 6. (a) Gibbs free energy diagrams for NiCo-LDH and NiCo-LDH@Sulfate in OER and CIOR. (b-c) The Bader charge of OH⁻ and ClO⁻ interactions, with yellow indicating the accumulation area of electrons and blue indicating the dissipation area of electrons. (d) Adsorption energies of *OH on the NiCo-LDH electrodes modified with various oxyanion films. (e) Illustration of Ni 3d (from NiCo-LDH) and O 2p (from *OH) band centers obtained by theoretical calculations of the models derived from NiCo-LDH electrode modified with various oxyanion films.

The mechanism for the selectivity between OER and CIOR of NiCo-LDH@Sulfate was studied by DFT calculations through calculating the Gibbs free energy change (ΔG) during the OER and CIOR processes (Fig. 6a). The relevant small-molecule adsorption models are shown in Fig. S25-S26. The ΔG for the most endothermic step for OER (*O → *OOH) is 1.91 eV for NiCo-LDH@Sulfate, which is lower than that of NiCo-LDH (2.19 eV), confirming that OER is thermodynamically more favorable on NiCo-LDH@Sulfate.⁶⁸ We also experimentally evaluated the OER activities of NiCo-LDH@Sulfate and NiCo-LDH in 1.0 M KOH (Fig. S27). The results showed that NiCo-LDH@Sulfate

exhibited higher inherent OER activity than NiCo-LDH in the absence of any interference with Cl⁻, consistent with the computational results. In contrast, the ΔG for the most thermodynamically uphill step for the CIOR process (*O → *OCl) on NiCo-LDH@Sulfate is 2.53 eV, higher than that of NiCo-LDH (2.17 eV). These results not only provide the reasons for the enhanced OER activity after surface modification with sulfate but also explain the inhibited CIOR activity and thusly enhanced stability during alkaline seawater splitting.

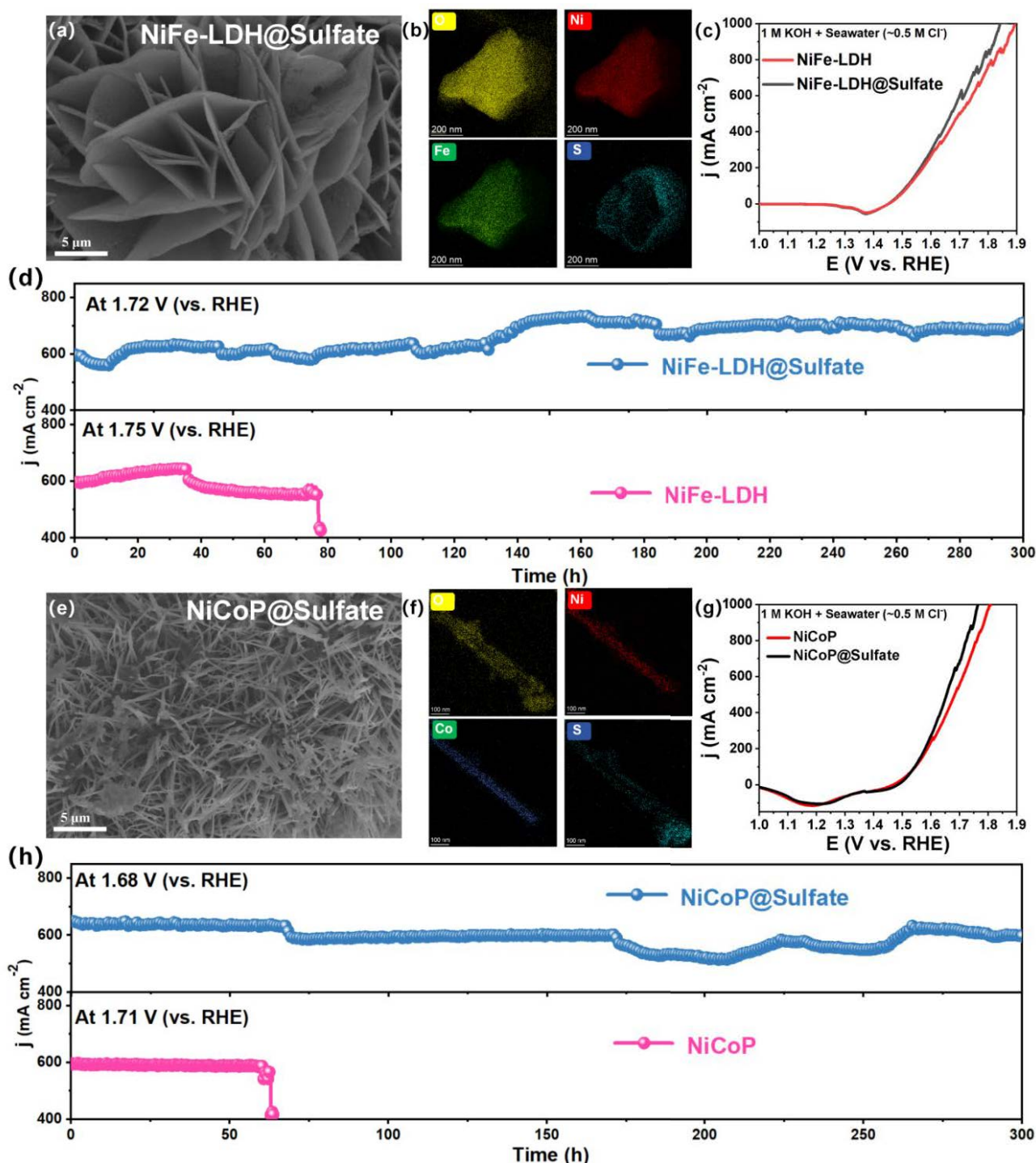


Fig. 7. Surface modification of sulfate on other OER catalysts. SEM (a) and EDX-mapping (b) images for NiFe-LDH@Sulfate. (c) LSV of NiFe-LDH@Sulfate and NiFe-LDH catalysts in 1 M KOH + seawater. (d) The constant potential tests of NiFe-LDH@Sulfate and NiFe-LDH to achieve similar current density of 600 mA cm^{-2} . SEM (e) and EDX-mapping (f) images for NiCoP@Sulfate. (g) LSV of NiCoP@Sulfate and NiCoP catalysts in 1 M KOH + seawater. (h) The constant potential tests of NiCoP@Sulfate and NiCoP to achieve similar current density of 600 mA cm^{-2} .

Given the inevitability of surface reconstruction during the OER, we also constructed atomic models of NiCoOOH@Sulfate and NiCoOOH (the post-reconstruction products, Fig. S28) and calculated their corresponding ΔG values for both the OER and CIOR processes. As shown in Fig. S29, the ΔG for the most endothermic step of OER and CIOR on NiCoOOH@Sulfate are 1.83 and 2.46 eV, respectively,

both slightly lower than those of NiCo-LDH@Sulfate (1.91 and 2.53 eV), indicating that reconstruction not only promotes the OER process but also facilitates CIOR to some extent. More importantly, compared to the bare NiCoOOH (ΔG are 2.01 and 2.12 eV for OER and CIOR), NiCoOOH@Sulfate is thermodynamically more favorable

for OER but less favorable for CIOR, which is consistent with the trend observed on NiCo-LDH@Sulfate (before reconstruction).

Furthermore, Bader charge analysis was utilized to determine the interactions of NiCo-LDH@Sulfate and NiCo-LDH with *OCl and *OH. As shown in Fig. 6b-c, the yellow areas represent electron accumulation, and the blue areas represent electron depletion. Upon surface modification with sulfate, the electron transfer between the catalyst and *ClO is suppressed, while the electron transfer between the catalyst and *OH is enhanced. This result reinforced that NiCo-LDH@Sulfate is more favorable for *OH adsorption (towards OER) and has a certain repelling effect for *ClO adsorption (towards CIOR). These computational studies collectively explain the excellent OER selectivity of NiCo-LDH@Sulfate in seawater splitting.⁶⁹

To gain a deeper understanding of the impact of oxyanion modification on the OER activity of NiCo-LDH electrodes, we calculated the adsorption energies of *OH, a key reaction intermediate. As shown in the Fig. 6d, the adsorption energy of *OH on the NiCo-LDH electrode (-0.05 eV) was enhanced after oxyanion modification, with NiCo-LDH@Sulfate exhibiting the strongest adsorption (-0.26 eV), followed by NiCo-LDH@Phosphate (-0.18 eV) and NiCo-LDH@Carbonate (-0.08 eV). The enhanced *OH adsorption was also validated by the *in-situ* infrared spectroscopy (Fig. S30-S31): with an increase of potential, the *OH signal on NiCo-LDH@Sulfate gradually increased, and the trend was significantly more pronounced than that of NiCo-LDH, which is consistent with the DFT results. We attribute the difference in *OH adsorption to the change of the coordination intensity between the active Ni sites and *OH upon the oxyanion formation.⁷⁰ As shown in Fig. 6e and S32, we calculated the band centers for Ni 3d ($E_{\text{Ni-3d}}$, from NiCo-LDH) and O 2p ($E_{\text{O-2p}}$, from adsorbed *OH). Among the four electrodes studied, the covalency energy ($\Delta\epsilon$) between the Ni and O sites in NiCo-LDH@Sulfate was found to be significantly stronger than the rest electrodes. The d-band center of the Ni sites was also closer to the Fermi level upon oxyanion modification, resulting a stronger *OH adsorption as well. These results suggest that the sulfate modification may have greater application potential among the three oxyanions.

3.5. Extension of the oxyanion modification strategy to other OER catalysts

To verify the broad applicability of the oxyanion surface modification strategy, we applied this technology to other OER catalysts. Based on previous reports, NiFe-LDH sheet array electrodes were synthesized and the surface was modified with a sulfate layer (NiFe-LDH@Sulfate).⁴¹ The successful synthesis of NiFe-LDH@Sulfate was confirmed through XRD, SEM, and TEM characterizations (Fig. 7a-b, S33-34 and Table S8). The electrochemical OER activity of NiFe-LDH@Sulfate was evaluated in alkaline seawater electrolyte (Fig. 7c). The NiFe-LDH@Sulfate required 440 mV and 610 mV to reach 500 mA cm⁻² and 1 A cm⁻², respectively, outperforming the unmodified NiFe-LDH (490 mV and 660 mV). Moreover, as shown in Fig. S35, NiFe-LDH@Sulfate maintained good activity and structural stability after 10,000 CV cycles. As shown in Fig. 7d, stability tests at a constant potential of 1.72 V vs. RHE demonstrated that NiFe-LDH@Sulfate could maintain high OER activity in alkaline seawater for over 300 hours without electrolyte recirculation, which is four times longer than NiFe-LDH (77 hours).

Similarly, NiCoP needle-like array electrodes were also synthesized and modified with a sulfate layer (NiCoP@Sulfate).⁴² The successful synthesis of NiFe-LDH@Sulfate was also confirmed through XRD, SEM, and TEM characterizations (Fig. 7e-f, S36-37 and Table S9). The electrochemical OER activity of NiCoP@Sulfate was evaluated in alkaline seawater electrolyte (Fig. 7g). The NiCoP@Sulfate required 415 mV and 533 mV to reach 500 mA cm⁻² and 1 A cm⁻², respectively, outperforming the unmodified NiCoP (453 mV and 580 mV). Moreover, as shown in Fig. S38, after 10,000 CV cycles, NiCoP@Sulfate retained excellent activity and structural stability. Furthermore, as shown in Fig. 7h, NiCoP@Sulfate could maintain high OER activity in alkaline seawater for over 300 hours without electrolyte recirculation, far exceeding NiCoP (63 hours). These results confirmed that the surface modification strategy involving electrodeposition of oxyanion films has a broad applicability to various array electrodes.

3.5. Overall seawater splitting performance

To further demonstrate the advanced electrocatalytic performance of NiCo-LDH@Sulfate, we conducted overall seawater splitting tests in a flow cell system (Fig. 8a). As shown in Fig. 8b, the flow-cell electrolyzer, employing NiCo-LDH@Sulfate as the anode and previously-reported Ni₂P/Co(PO₃)₂ as the cathode⁷¹, exhibited exceptional performance for overall seawater splitting. Specifically, it required only 1.78 V and 1.93 V vs. RHE to achieve current densities of 600 mA cm⁻² and 1000 mA cm⁻², respectively. Impressively, the system also demonstrated remarkable electrolysis stability, operating continuously for over 1000 hours at 600 mA cm⁻² without obvious performance degradation. These results highlight the outstanding practical applicability of NiCo-LDH@Sulfate as an anode catalyst for overall seawater splitting.

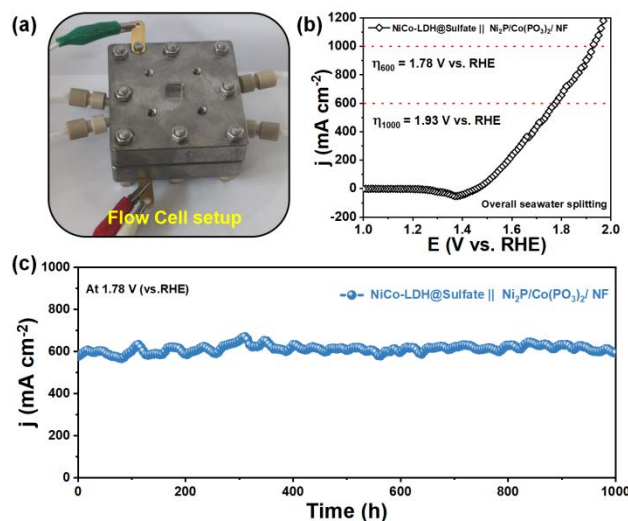


Fig. 8. (a) Photo showing the flow cell electrolysis system for electrocatalytic seawater splitting. (b) LSV curves for overall seawater splitting in a flow-cell electrolyzer using NiCo-LDH@Sulfate as the anode and Ni₂P/Co(PO₃)₂ as the cathode in 1 M KOH + seawater. (c) The corresponding i-t stability test for the electrolyzer.

4. Conclusions

In summary, a universal strategy for the surface modification involving the electrodeposition of oxyanion films (sulfate, phosphate and carbonate) has been developed, which can protect OER-active centers from the influence of Cl^- during seawater splitting. Among the three oxyanion films, sulfate modification demonstrated the best seawater electrolysis activity and stability. The 5-min electrodeposited NiCo-LDH@Sulfate catalyst can achieve 1 A cm^{-2} with an overpotential of only 381 mV and maintain stable OER activity at 600 mA cm^{-2} for over 330 hours in alkaline seawater. By combining in-situ characterizations, probe techniques, and theoretical calculations, we explored the ClOR-inhibiting and OER-facilitating effects of the oxyanion film: the high surface electrostatic potential of the oxyanion films can effectively repel Cl^- ; the oxyanion modification can also adjust the binding intensity between the OER catalytic center and $^*\text{OH}$ to enhance $^*\text{OH}$ adsorption and suppress $^*\text{ClO}$ adsorption. In particular, we identified that sulfate modification endows the catalysts with the highest surface anion loading, the most negative electrostatic potential, and the strongest adsorption of $^*\text{OH}$, which accounts for its superior seawater electrolysis performance. Very attractively, this electrodeposition strategy has a broad applicability for different anions and OER catalysts. Apparently, this study demonstrated a rapid and effective preparation strategy for seawater splitting anode catalysts and shed new light on the industrialization of seawater splitting.

Author contributions

Meng Zhang: Software, Data curation, Investigation, Writing-original draft. Yuzhu Sun: Software, Data curation, Investigation. Chenchen Meng: Software, Data curation. Qijun Xu: Investigation. Yang Zhang: Writing-review & editing. Xiaohong Li: Writing-review & editing. Louzhen Fan: Writing-review & editing. Tengfei Li: Conceptualization, Writing-review & editing. Yunchao Li: Supervision, Conceptualization, Writing-review & editing, Project administration. Meng Zhang and Yuzhu Sun contributed equally to this work.

Conflicts of interest

There are no conflicts to declare.

Data availability

The data supporting this article have been included as part of the Experimental section and Supplementary Information.

Acknowledgements

This work was financially supported by the National Natural Science Foundation of China (Nos. 22272008 and 21872011) and the Royal Society of Chemistry Researcher Collaborations Grant (C23-2829295121).

References

- 1 N. Höhne, M. J. Gidden, M. den Elzen, F. Hans, C. Fyson, A. Geiges, M. L. Jeffery, S. Gonzales-Zuñiga, S. Mooldijk, W. Hare and J. Rogelj, *Nat. Clim. Chang.*, 2021, **11**, 820-822.
- 2 W. Tong, M. Forster, F. Dionigi, S. Drespe, R. Sadeghi Erami, P. Strasser, A. J. Cowan and P. Farràs, *Nat. Energy.*, 2020, **5**, 367-377.
- 3 F. Sun, J. Qin, Z. Wang, M. Yu, X. Wu, X. Sun and J. Qiu, *Nat. Commun.*, 2021, **12**, 4182.
- 4 J. Tian, Q. Liu, A. M. Asiri and X. Sun, *J. Am. Chem. Soc.*, 2014, **136**, 7587-7590.
- 5 Z. W. Seh, J. Kibsgaard, C. F. Dickens, I. Chorkendorff, J. K. Nørskov and T. F. Jaramillo, *Science*, 2017, **146**, 355.
- 6 R. Fan, C. Liu, Z. Li, H. Huang, J. Feng, Z. Li and Z. Zou, *Nat. Sustain.*, 2024, **7**, 158-167.
- 7 Z. J. Zhao, H. Zhao, X. Q. Du and X. S. Zhang, *Int. J. Hydrogen Energy.*, 2024, **88**, 313 – 321.
- 8 Y. H. Wang, S. J. Liu, X. Q. Du, X. S. Zhang, *Int. J. Hydrogen Energy.*, 2024, **88**, 450 – 461.
- 9 Y. Kuang, M. J. Kenney, Y. Meng, W. H. Hung, Y. Liu, J. E. Huang, R. Prasanna, P. Li, Y. Li, L. Wang, M. C. Lin, M. D. McGehee, X. Sun and H. Dai, *Proc. Natl. Acad. Sci. USA.*, 2019, **116**, 6624-6629.
- 10 Y. Y. Ma, C. X. Wu, X. J. Feng, H. Q. Tan, L. K. Yan, Y. Liu, Z. H. Kang, E. B. Wang and Y. G. Li, *Energy Environ. Sci.*, 2017, **10**, 788-798.
- 11 H. Jing, W. Li, Y. Lin, J. Y. Duan, Q. L. Wen, Y. W. Liu and T. Y. Zhai, *Chem. Soc. Rev.*, 2024, **23**, 10709-10740.
- 12 H. Y. Chen, R. T. Gao, H. J. Chen, Y. Yang, L. M. Wu and L. Wang, *Adv. Funct. Mater.*, 2024, **34**, 2315674.
- 13 S. Zhang, Y. Wang, S. Li, Z. Wang, H. Chen, L. Yi, X. Chen, Q. Yang, W. Xu, A. Wang and Z. Lu, *Nat. Commun.*, 2023, **14**, 4822.
- 14 S. C. Li, T. Liu, W. Zhang, M. Z. Wang, H. J. Zhang, C. L. Qin, L. Zhang, Y. D. Chen, S. W. Jiang, D. Liu, X. K. Liu, H. J. Wang, Q. Q. Luo, T. Ding and T. Yao, *Nat. Commun.*, 2024, **15**, 3416.
- 15 Y. J. Bao, H. F. Ru, Y. F. Wang, K. X. Zhang, R. T. Yu, Q. Wu, A. M. Yu, D. S. Li, C. H. Sun, W. W. Li and J. C. Tu, *Adv. Funct. Mater.* 2024, **34**, 2314611.
- 16 Y. Chen, Y. Liu, W. Zhai, H. Liu, T. Sakthivel, S. Guo and Z. Dai, *Adv. Energy Mater.*, 2024, **14**, 202400059.
- 17 X. Lu, Z. Ma, Y. Chang, S. Wang, X. Li, D. Xu, J. Bao and Y. Liu, *Adv. Mater.*, 2024, **36**, 202313057.
- 18 L. Lei, D. Huang, C. Zhou, S. Chen, X. Yan, Z. Li and W. Wang, *Coord. Chem. Rev.*, 2020, **408**, 213177.
- 19 R. Gao and D. Yan, *Adv. Energy Mater.*, 2019, **10**, 1900954.
- 20 J. Hu, X. Tang, Q. Dai, Z. Liu, H. Zhang, A. Zheng, Z. Yuan and X. Li, *Nat. Commun.*, 2021, **12**, 3409.
- 21 S. H. Hsu, J. Miao, L. Zhang, J. Gao, H. Wang, H. Tao, S. F. Hung, A. Vasileff, S. Z. Qiao and B. Liu, *Adv. Mater.*, 2018, **30**, 1707261.
- 22 W. Xu, T. Ma, H. Chen, D. Pan, Z. Wang, S. Zhang, P. Zhang, S. Bao, Q. Yang, L. Zhou, Z. Tian, S. Dai and Z. Lu, *Adv. Funct. Mater.*, 2023, **33**, 2302263.
- 23 X. Q. Du, Y. Y. Ding and X. S. Zhang, *Green Energy Environ.*, 2023, **8**, 798 – 811.
- 24 Y. Cao, T. Wang, X. Li, L. C. Zhang, Y. L. Luo, F. Zhang, A. M. Asiri, J. M. Hu, Q. Liu and X. P. Sun, *Inorg. Chem. Front.*, 2021, **8**, 3049 – 3054.
- 25 L. L. Liao, D. Y. Li, Y. Zhang, Y. Zhang, F. Yu, L. Yang, X. Z. Wang, D. S. Tang and H. Q. Zhou, *Adv. Mater.*, 2024, **36**, 2405852.
- 26 Y. Liu, Y. Wang, P. Fornasiero, G. Tian, P. Strasser and X. Y. Yang, *Angew. Chem. Int. Ed.*, 2024, **63**, 202412087.
- 27 N. Wang, P. Ou, S. F. Hung, J. E. Huang, A. Ozden, J. Abed, I. Grigioni, C. Chen, R. K. Miao, Y. Yan, J. Zhang, Z. Wang, R.

- Dorakhan, A. Badreldin, A. Abdel-Wahab, D. Sinton, Y. Liu, H. Liang and E. H. Sargent, *Adv. Mater.*, 2023, **35**, 2210057.
- 28 H. Xie, Z. Zhao, T. Liu, Y. Wu, C. Lan, W. Jiang, L. Zhu, Y. Wang, D. Yang and Z. Shao, *Nature*, 2022, **612**, 673-678.
- 29 J. Chang, G. Wang, Z. Yang, B. Li, Q. Wang, R. Kuliev, N. Orlovskaya, M. Gu, Y. Du, G. Wang and Y. Yang, *Adv. Mater.*, 2021, **33**, 2101425.
- 30 S. Pal, K. Shimizu, S. Khatun, S. Singha, S. Watanabe and P. Roy, *J. Mater. Chem. A.*, 2023, **11**, 12151-12163.
- 31 H. J. Song, H. Yoon, B. Ju, D. Y. Lee and D. W. Kim, *ACS Catal.*, 2019, **10**, 702-709.
- 32 Z. W. Cai, J. Liang, Z. X. Li, T. Y. Yan, C. X. Yang, S. J. Sun, M. Yue, X. W. Liu, T. Xie, Y. Wang, T. S. Li, Y. S. Luo, D. D. Zheng, Q. Liu, J. X. Zhao, X. P. Sun and B. Tang, *Nat. Commun.*, 2024, **15**, 6624.
- 33 H. C. Chen, P. Y. Liu, W. B. Li, W. W. Xu, Y. J. Wen, S. X. Zhang, L. Yi, Y. P. Dai, X. Chen, S. Dai, Z. Q. Tian, L. Chen and Z. Y. Lu, *Adv. Mater.*, 2024, **36**, 2411302.
- 34 Z. Li, Y. Yao, S. Sun, J. Liang, S. Hong, H. Zhang, C. Yang, X. Zhang, Z. Cai, J. Li, Y. Ren, Y. Luo, D. Zheng, X. He, Q. Liu, Y. Wang, F. Gong, X. Sun and B. Tang, *Angew. Chem. Int. Ed.*, 2023, **63**, 202316522.
- 35 Z. B. Liu, Y. Y. Li, L. B. Zeng, X. Y. Peng, D. S. Wang, Z. J. Li, B. Yang, Y. Y. Li, L. C. Lei and Y. Hou, *Adv. Funct. Mater.*, 2024, **34**, 2407781.
- 36 L. Yu, Q. Zhu, S. W. Song, B. McElhenny, D. Z. Wang, C. Z. Wu, Z. J. Qin, J. M. Bao, Y. Yu, S. Chen and Z. F. Ren, *Nat. Commun.*, 2019, **10**, 5106.
- 37 L. L. Guo, J. Q. Chi, T. Cui, J. W. Zhu, Y. N. Xia, H. L. Guo, J. P. Lai and L. Wang, *Adv. Energy Mater.*, 2024, 2400975.
- 38 T. T. Fang, X. Yu, X. Z. Han, J. Gao and Y. R. Ma, *Small*, 2024, 2402478.
- 39 M. Z. Li, H. J. Niu, Y. L. Li, J. W. Liu, X. Y. Yang, Y. Z. Lv, K. P. Chen and W. Zhou, *Appl. Catal. B Environ.*, 2023, **330**, 122612.
- 40 T. Cui, J. Q. Chi, J. W. Zhu, X. M. Sun, J. P. Lai, Z. J. Li and L. Wang, *Appl. Catal. B Environ.*, 2022, **319**, 121950.
- 41 F. Ning, M. Shao, S. Xu, Y. Fu, R. Zhang, M. Wei, D. G. Evans and X. Duan, *Energy Environ. Sci.*, 2016, **9**, 2633-2643.
- 42 Z. Zhan, S. Zhang, Y. Du, P. Yin and T. Lei, *Energy Fuels*, 2022, **36**, 8371-8380.
- 43 T. Wang, M. Kunimoto, T. Mori, M. Yanagisawa, J. Niikura, I. Takahashi, M. Morita, T. Abe and T. Homma, *J. Power Sources*, 2022, **533**, 231237.
- 44 S. Zhou, J. Wang, J. Li, L. Fan, Z. Liu, J. Shi and W. Cai, *Appl. Catal. B Environ.*, 2023, **332**, 122749.
- 45 M. Bakhtbidar, I. Amaechi, A. Dörfler, A. Merlen and A. Ruediger, *Adv. Mater. Interfaces*, 2024, **11**, 2300993.
- 46 H. Zhang, H. Guo, Y. Li, Q. Zhang, L. Zheng, L. Gu and R. Song, *Adv. Funct. Mater.*, 2023, **33**, 2304403.
- 47 M. Zhang, W. Z. Chen, Z. L. Liu, J. He and Y. Q. Wang, *Electrochim. Acta*, 2022, **433**, 141269.
- 48 G. J. Wang, Y. Z. Sun, Y. D. Zhao, Y. Zhang, X. H. Li, L. Z. Fan and Y. C. Li, *Nano Res.*, 2022, **15**, 8771-8782.
- 49 P. Guo, S. Cao, W. Huang, X. Lu, W. Chen, Y. Zhang, Y. Wang, X. Xin, R. Zou, S. Liu and X. Li, *Adv. Mater.*, 2024, **36**, 2311766.
- 50 Y. Xie, Y. Feng, S. Pan, H. Bao, Y. Yu, F. Luo and Z. Yang, *Adv. Funct. Mater.*, 2024, **34**, 2406351.
- 51 H. Luo, S. Li, Z. Wu, M. Jiang, M. Kuang, Y. Liu, W. Luo, D. Zhang and J. Yang, *Adv. Funct. Mater.*, 2024, 2403838. DOI: 10.1002/adfm.202403838.
- 52 K. Fan, L. Zong, J. Liu, C. H. Chuang, M. Dong, Y. Zou, Y. Xu, H. Q. Fu, L. Zhang, L. Wang, M. Zhou, T. Zhan, P. Liu and H. Zhao, *Adv. Energy Mater.*, 2024, **14**, 2400052.
- 53 X. Ding, D. Liu, P. Zhao, X. Chen, H. Wang, F. E. Oropeza, G. Gorni, M. Barawi, M. García-Tecedor, V. A. de la Peña O'Shea, J. P. Hofmann, J. Li, J. Kim, S. Cho, R. Wu and K. H. L. Zhang, *Nat. Commun.*, 2024, **15**, 5336.
- 54 Y. Sun, S. Sun, H. Yang, S. Xi, J. Gracia and Z. J. Xu, *Adv. Mater.*, 2020, **32**, 2003297.
- 55 J. O' M. Bockris and T. Otagawa, *J. Phys. Chem.*, 1983, **57**, 2960-2971.
- 56 X. Li, W. C. Zhu, F. Yue, H. J. Pang, C. T. Wang, D. J. Wang, Y. X. Lu, C. M. Yang, *Appl. Catal. B Environ.*, 2024, **358**, 124418.
- 57 H. Jin, J. Xu, H. Liu, H. Shen, H. Yu, M. Jaroniec, Y. Zheng and S. Z. Qiao, *Sci. Adv.*, 2023, **9**, 7755.
- 58 S. Lee, K. Banjac, M. Lingenfelder and X. Hu, *Angew. Chem. Int. Ed.*, 2019, **58**, 10295-10299.
- 59 M. V. Castillo, M. A. Iramain, L. Davies, M. E. Manzur and S. A. Brandán, *J. Mol. Struct.*, 2021, **1228**, 129795.
- 60 C. C. Jiang, X. C. Li, J. A. Fan, J. Y. Fu, X. N. H. Fu, J. J. Li, J. F. Zheng, X. S. Zhou and Y. H. Wang, *Analyst.*, 2022, **147**, 1341-1347.
- 61 Y. Song, M. Sun, S. Zhang, X. Zhang, P. Yi, J. Liu, B. Huang, M. Huang and L. Zhang, *Adv. Funct. Mater.*, 2023, **33**, 2214081.
- 62 H. Zhang, X. He, K. Dong, Y. Yao, S. Sun, M. Zhang, M. Yue, C. Yang, D. Zheng, Q. Liu, Y. Luo, B. Ying, S. Alfaifi, X. Ji and B. Tang, *X. Sun, Mater. Today Phys.*, 2023, **38**, 101249.
- 63 G. Bahuguna, B. Filanovsky and F. Patolsky, *Nano Energy*, 2023, **111**, 108439.
- 64 H. M. Haynes, *Handbook of Chemistry and Physics*, 95th ed.; CRC Press: Boca Raton, FL, 2014.
- 65 H. Li, B. S. Chang, H. Kim, Z. Xie, A. Lainé, L. Ma, T. Xu, C. Yang, J. Kwon, S. W. Shelton, L. M. Klivansky, V. Altoé, B. Gao, A. M. Schwartzberg, Z. Peng, R. O. Ritchie, T. Xu, M. Salmeron, R. Ruiz, K. B. Sharpless, P. Wu and Y. Liu, *Joule*, 2023, **7**, 95-111.
- 66 N. Wang, Z. Cao, X. Zheng, B. Zhang, S. M. Kozlov, P. Chen, C. Zou, X. Kong, Y. Wen, M. Liu, Y. Zhou, C. T. Dinh, L. Zheng, H. Peng, Y. Zhao, L. Cavallo, X. Zhang and E. H. Sargent, *Adv. Mater.*, 2020, **32**, 1906806.
- 67 P. Berruyer, C. Cibaka-Ndaya, A. Pinon, C. Sanchez, G. L. Drisko and L. Emsley, *J. Am. Chem. Soc.*, 2023, **145**, 9700-9707.
- 68 X. Duan, Q. Sha, P. Li, T. Li, G. Yang, W. Liu, E. Yu, D. Zhou, J. Fang, W. Chen, Y. Chen, L. Zheng, J. Liao, Z. Wang, Y. Li, H. Yang, G. Zhang, Z. Zhuang, S. F. Hung, C. Jing, J. Luo, L. Bai, J. Dong, H. Xiao, W. Liu, Y. Kuang, B. Liu and X. Sun, *Nat. Commun.*, 2024, **15**, 1973.
- 69 F. Zhang, L. Gong, M. Liu, Y. Ying, Y. Cui, J. Shao, Y. Yu, A. Gao, J. Ma and L. Zhang, *Nano Energy*, 2024, **127**, 109699.
- 70 X. L. Wang, R. G. Ma, S. L. Li, M. M. Xu, L. J. Liu, Y. H. Feng, T. J. Thomas, M. H. Yang and J. C. Wang, *Adv. Energy Mater.*, 2023, **13**, 2300765.
- 71 M. Zhang, W. Z. Chen, Z. L. Liu, J. L. He and Y. Q. Wang, *Int. J. Hydrogen Energ.*, 2023, **48**, 17783-17800.